Phase transformation barrier modulation of $CsPbI_3$ films via PbI_3^- complex for efficient all-inorganic perovskite photovoltaics

Nano Energy 99 (2022) 107388

Contents lists available at ScienceDirect

Nano Energy

journal homepage: www.elsevier.com/locate/nanoen

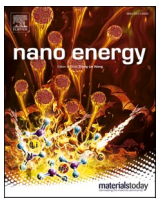

Phase transformation barrier modulation of $CsPbI_3$ films via PbI_3^- complex for efficient all-inorganic perovskite photovoltaics

Zhiwen Qiu [a,1], Feng Wang [a,1], Chenyue Wang [b,c], Cheng Zhu [b], Hao Wang [b], Qi Chen [b], Yihua Chen [a], Yu Zhang [a], Zhenyu Guo [a], Nengxu Li [a], Huachao Zai [a], José Manuel Vicent-Luna [d], Shuxia Tao [d], Huanping Zhou [a,*]

[a] School of Materials Science and Engineering, Peking University, Beijing 100871, PR China
[b] Department of Materials Science and Engineering, Beijing Institute of Technology, Beijing 100081, PR China
[c] Radiation Facility (SSRF), Zhangjiang Laboratory, Shanghai Advanced Research Institute, Chinese Academy of Sciences, 239 Zhangheng Road, Shanghai 201204, China
[d] Materials Simulation and Modelling, Department of Applied Physics and Center for Computational Energy Research, Department of Applied Physics, Eindhoven University of Technology, 5600 MB Eindhoven, The Netherlands

ARTICLE INFO

Keywords:
Cesium lead iodide
Phase transformation
Stoichiometry modulation
Pb−I complex

ABSTRACT

Cesium lead iodide ($CsPbI_3$) has gained great attention due to its thermal stability and appropriate bandgap (≈1.73 eV) at black (γ) phase potentially suitable for tandem solar cells. However, it is challenging to obtain $CsPbI_3$ film with desired black phase. Herein, we fabricate kinetically favorable γ-$CsPbI_3$ thin films by stoichiometry modulation, where in-situ 2D GIWAXS measurement was innovatively performed to illustrate the phase transition process of the precursor films, to aid a full picture study on the entire film evolution process. Conceptually different from introducing other extrinsic species, the cogenetic doping by excessive cesium iodide is found to tailor energy barriers for phase transformations during both the film formation and ageing process simultaneously. During film growth, excessive CsI affects the formation of Pb−I complex in the precursor solution, which facilitates the δ to γ phase transformation. Also, the Cs-rich resultant film could suppress γ to δ phase transformation. The corresponding $CsPbI_3$ solar cells deliver a PCE of 16.68% without performance loss at continuous maximum power point output (MPP) for ~175 h under continuous illumination in a N_2 glovebox. This work highlights the importance of precursors chemistry and provides guidelines to adjust the phase transformation barrier in $CsPbI_3$ films without any foreign additives.

1. Introduction

Over the past decade, unprecedented efficiency progress of hybrid organic–inorganic perovskite solar cells (PSCs) have been witnessed from an unstable 3.8% to certified 25.2%. [1,2] Inorganic PSCs, e.g. $CsPbI_3$, have lately drawn tremendous attention due to their potentially better thermal stability. [3] Additionally, the optical bandgap of $CsPbI_3$ is 1.73 eV, [4] an ideal absorber for the construction of tandem solar cells by working with silicon or other low bandgap materials. Unfortunately, the improper tolerance factor allows a kinetically favorable formation of undesired non-photoactive yellow phase (δ) during film growth, and an easier transformation from photoactive black $CsPbI_3$ to yellow under the ageing conditions. The presence of δ phase is detrimental to photoelectric conversion process for $CsPbI_3$ solar cells. [5,6] In addition, a highly crystalline, spatially uniform $CsPbI_3$ film cannot be easily prepared due to the low mass transport and diffusion. [7] In this regard, it is important to obtain high quality films with favored crystallization, phase evolution kinetics, minimized charge traps and structural defects, which is essential to lower carrier recombination rate and improve device performance. [8].

Various approaches have been investigated to prepare highly crystalline $CsPbI_3$ film so far.[9−20] For instance, the incorporation of a small amount of hydriodic acid (HI) in the precursor solution is the most common approach to facilitate the conversion from δ to γ phase at relatively low temperature (<200 ℃). [9] This is likely due to either the generation of lattice strain associated with the formation of small

* Corresponding author.
E-mail address: happy_zhou@pku.edu.cn (H. Zhou).
[1] *These authors contributed equally to this work.*

https://doi.org/10.1016/j.nanoen.2022.107388
Received 1 January 2022; Received in revised form 14 May 2022; Accepted 16 May 2022
Available online 20 May 2022

perovskite crystals by HI, or the more desirable tolerance factor of perovskite phase by the employment of large cation DMA that formed via the decomposition of DMF induced by HI. [10] Also, many other doping methods have been used to stabilize the phase of $CsPbI_3$ at lower temperature by tuning the tolerance factor or surface energy, for example, the partial substitution of iodide by bromide ($CsPbI_{3-x}Br_x$), [11–17] or the introduction of strontium, [17] bismuth, [18] sulfobetaine zwitterions, [19] and phenethylamine (PEA). [20] However, the above studies require the assistance from organic additives or foreign elements which may adversely affect the thermal and/or the light stability. Interestingly, high quality black phase $CsPbI_3$ can be obtained at low temperature or even at room temperature by simply adjusting the precursor stoichiometry without the involvement of foreign additives,[21–23] e.g. the ratio of CsI/PbI_2. However, little research has been reported regarding the relationship between the colloidal intermediates in the precursor composed of polyiodide complexes, [24]

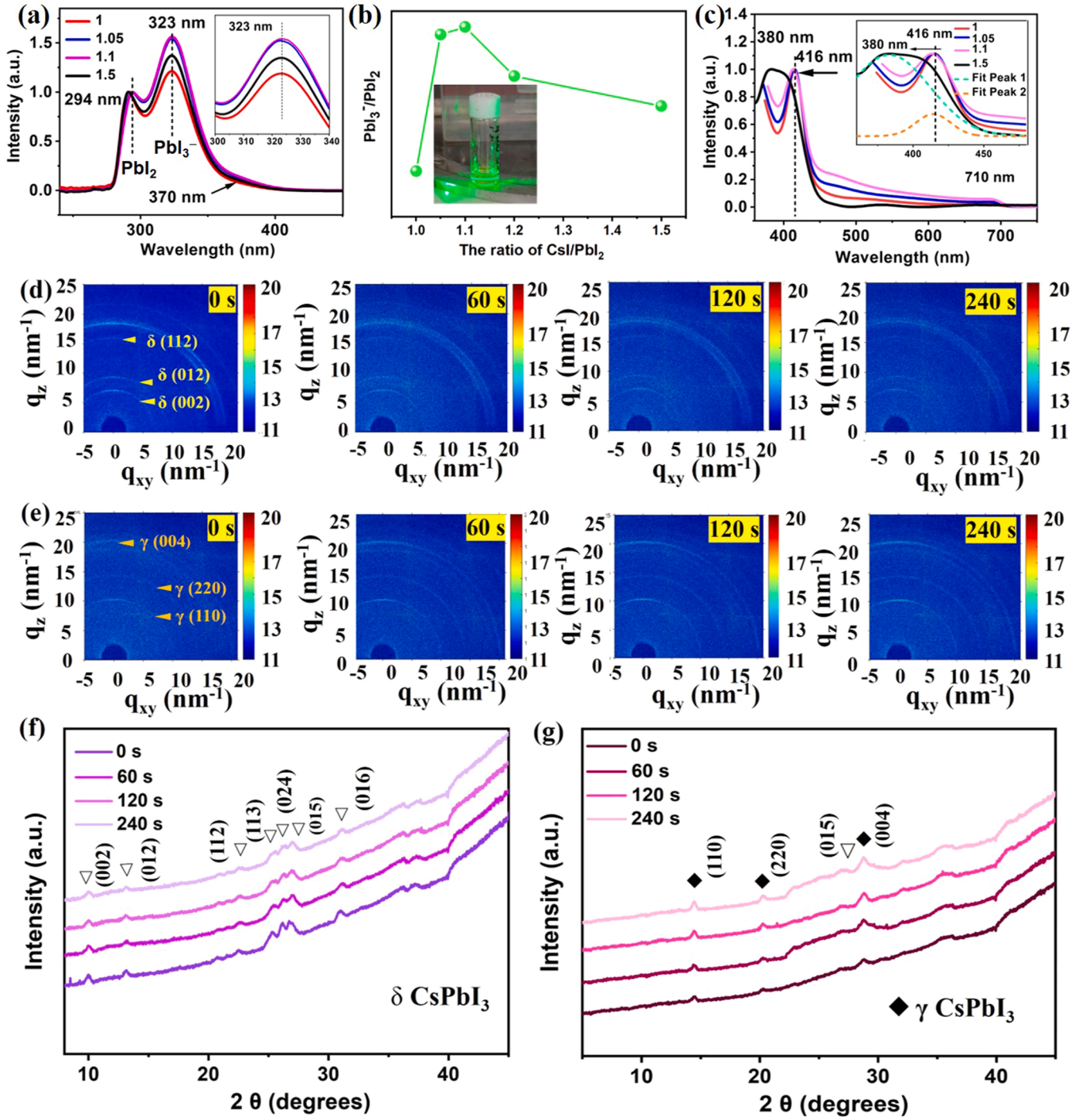

Fig. 1. (a) UV−Vis absorption spectra of perovskite precursors with different stoichiometric ratios of CsI/PbI_2 varied from 1 to 1.5, the inset is locally magnified spectra at 323 nm. b) the ratio of PbI_3^-/PbI_2 verse different perovskite precursors, the inset is tyndall effect photographs of the 1.1 CsI/PbI_2 precursor solution. c) UV−Vis absorption spectra of the corresponding perovskite precursor films, the inset is the locally magnified spectra. 2D GIWAXS patterns for perovskite formations at different crystallization stages versus spin-coating time (0 s and 240 s): $CsI/PbI_2 = 1$ and 1.1 for d) and e), respectively. f−g) 1D GIWAXS 2θ signals generated from 2D GIWAXS patterns (e−f) respectively.

such as $[PbI_2]$, $[PbI_3]^-$, $[PbI_4]^{2-}$ and crystallization kinetics, the consequent morphology and phase evolution in $CsPbI_3$ perovskite. So, it is crucial to provide a clear and full picture from the precursor solution, to the solvated intermediate, and the perovskite solid, that govern the phase transformation of $CsPbI_3$ film and the resulting optoelectronic properties.

Herein, we performed a thorough analysis to systematically understand the formation process and kinetics of $CsPbI_3$ materials from precursor solution to final film by fine varying the stoichiometry of CsI/PbI_2. In particularly, in−situ grazing incidence wide−angle X − ray scattering (GIWAXS) was conducted to reveal the relationship between precursor stoichiometry, varied polyiodide complexes in the precursor solution, and phase evolution of $CsPbI_3$ in the solvated intermediate and final film. The excessive CsI would promote the formation of γ-phase $CsPbI_3$. An appropriate excessive CsI is found to affect the phase transformation kinetics, not only promoting the phase transition from δ to γ in film formation process, but also retarding the phase transition from γ to δ in the ageing process, that largely affect the resulting optoelectronic properties. As a result, the excessive CsI modified $CsPbI_3$ perovskite solar cell delivers a PCE of 16.68% and a good long-term operational stability with negligible degradation drop at the maximum power point under continuous illumination for ~175 h.

2. Results and discussion

Herein, we carried out a full picture study to investigate the effect of excessive CsI on the state of the precursor solution, the precursor films, and the annealed final perovskite films. The detailed experiment description is shown in SI. Briefly, we defined the samples of the ratio of CsI/PbI_2 = 1, 1.05,1.1, 1.5, 4 as 1 CsI/PbI_2, 1.05 CsI/PbI_2, 1.1 CsI/PbI_2, 1.5 CsI/PbI_2, 4 CsI/PbI_2. UV–vis spectroscopy measurements were conducted using diluted precursor solutions to avoid the strong absorption of Pb−I complex in the precursors, [24] shown in Fig. 1a−b and Fig. S1−S2 in the SI. Three peaks located at 294 nm, 323 nm, and 370 nm were attributed to PbI_2, PbI_3^-, and PbI_4^{2-} frameworks, respectively (Fig. 1a). [24] Fig. S2 showed the statistical distribution of the ratio of PbI_3^-/PbI_2 verse different perovskite precursors varied from 1 to 1.5. Interestingly, compared to the reference, all samples with excessive CsI showed increased absorption intensity of PbI_3^- complex. The intensity ratio of PbI_3^-/PbI_2 was closely related to the stoichiometric ratio of CsI/PbI_2, which maximized when the stoichiometric ratio reached 1.1. Meanwhile, we carried out molecular dynamics (MD) simulations using the density functional tight-binding method (Fig. S3−S5). When using CsI/PbI_2 = 1, we found that the clusters are mainly linear arrangements of PbI_x complexes surrounded Cs cations. Despite the differences, these linear distributions of PbI_x complexes in a given direction resemble the structure of the yellow $CsPbI_3$ (δ) structure. For Cs-rich precursor solution system, we found the formation of a more 3-dimensional perovskite clusters where Cs atoms directly face to the PbI_x complexes. [25] This theoretical calculation further indicates the connection mode of Pb−I octahedral changed from edge− to corner− sharing, illustrating that the polyiodide complexes evolved from PbI_2 to PbI_3^-. The inclusion of these Cs atoms within the PbI_x complexes can favor the crystallization of the 3D γ-$CsPbI_3$, but hinders the formation of the δ-$CsPbI_3$ (Fig. S5). Furthermore, the maximized ratio of PbI_3^-/PbI_2 appears at 1.1 CsI/PbI_2, suggests the stronger interaction between Cs^+ and the inorganic frameworks, which is in coincide with the higher surface tension, derived from contact angle measurements of the precursor droplets shown in Fig. S6. The underlying mechanism will be further discussed later. From Fig. S7, we observed that the black γ-$CsPbI_3$ was formed faster from all the excessive CsI samples compared to the reference (1 CsI/PbI_2). This is likely due to that more PbI_3^- complexes may act as pre-nucleation sites, facilitating the phase transformation from yellow δ to black γ-$CsPbI_3$. [23] However, incorporation of too much CsI will further promote the formation of Cs_4PbI_6 cluster rather than the desired γ-$CsPbI_3$.[26] Also, with the increase of the excessive CsI, the PbI_2 peak had a tendency to red-shift first, maximizing at 1.1 CsI/PbI_2, followed by a blue shift. The phenomenon was closely related to the size of colloidal particles, [27] also evidenced by the dynamic light scattering (Fig. S7 and Table S2). This further confirms the fact that appropriate excessive CsI will affect the complex type and colloidal size. In addition, we analyzed the corresponding precursor film without annealing (Fig. 1c and Fig. S8). All samples showed two main peaks located at 416 nm and 710 nm, which were attributed to δ and black phase $CsPbI_3$, respectively. Interestingly, 1.1 CsI/PbI_2 sample showed the strongest signal of black phase $CsPbI_3$, compared to that with other ratios. To be noted, when CsI is excessive, the peak at 416 nm becomes asymmetric, suggesting the potential coexistence of multiple phases. This is clearly manifested in 1.5 CsI/PbI_2 (Fig. 1c), where the above asymmetric peak shifted to 380 nm divided into two peaks, one at 380 nm (γ-Cs_4PbI_6) and the other one at 416 nm (δ-$CsPbI_3$). In−situ 2D GIWAXS measurement, which has not been employed before in $CsPbI_3$ materials system, was performed to illustrate the phase transition process of the precursor films. The data were collected when the precursor film experiencing solvent evaporation during spin-coating process, and the detailed description was shown in Supporting Information. The 2D GIWAXS patterns and the derived 1D results were exhibited in Fig. 1d−e, Fig. S9 and Fig. 1 g−h accordingly. The details about the diffraction peaks were summarized in Table S3. The diffraction peaks located at 10.03°, 13.17°, 22.53°, 25.55°, 26.30°, 26.98°, 31.12°, corresponding to the (002), (012), (112), (113), (024), (015), (016) planes were ascribed to the yellow δ-phase $CsPbI_3$ (Fig. 1 f).[21,22] Along with the spin-coating lasting from 0 s to 240 s, only δ-$CsPbI_3$ exists in the precursor film for the 1 CsI/PbI_2 sample. Interestingly, the 1.1 CsI/PbI_2 sample showed dramatically different diffraction peaks that mainly located at 14.48°, 20.34°, 28.81°, corresponding to the (110), (220) and (004) planes for the $CsPbI_3$ distorted black perovskite phase (γ). [28,29] During the entire spin-coating process, the intensity of these diffraction peaks for black γ-$CsPbI_3$ enhanced gradually, except for a tiny amount of yellow δ-$CsPbI_3$ appeared at 240 s. These observations indicated that the 1.1 CsI/PbI_2 sample preferentially formed the γ phase, where the 1 CsI/PbI_2 formed the δ-phase. When the amount of CsI is continuously increased, many non-optically active Cs_4PbI_6 phase will generated, which are not ideal for the all-inorganic perovskite photovoltaics. For the 4 CsI/PbI_2 system, the main diffraction peaks are ascribed to Cs_4PbI_6 (Fig. S9).

GIWAXS measurements were further used to precisely investigate the impact of the excessive CsI on the final film in terms of phase, the crystal orientation in Fig. 2 and Fig. S10. It is noted that the samples were unencapsulated and measured in the 20–30% RH ambience. For the reference and 1.05 CsI/PbI_2 sample (Fig. 2a−b), the strong diffraction ring at q ≈ 10 nm^{-1} and 20 nm^{-1} are denoted as the characteristic diffraction peaks of γ-$CsPbI_3$ (110) and (220),[28] where q is the scattering vector ($q = 4\pi\sin\theta/\lambda$). Besides, the weak diffraction rings at q ≈ 7 nm^{-1} and 8.4 nm^{-1} are ascribed as the characteristic diffraction peaks of δ-$CsPbI_3$ (002) and (012). The phenomena show that the corresponding films have two different phases (γ and δ). This is associated to the fact that black phase γ-$CsPbI_3$ can't resist the invasion of H_2O molecules, which partially transformed into the δ-$CsPbI_3$. Encouragingly, with the increase of excessive CsI (CsI/PbI_2 =1.1, 1.5, 3, 4), the diffraction rings of δ-$CsPbI_3$ disappear (Fig. 2c−d). Meanwhile, more new diffraction peaks at 12.1°, 21.1°, 25.9°, 27.1°, 28.6° appear, which can be assigned to the (012), (300), (131), (214), (223) of the 0 D trigonal Cs_4PbI_6 film (R-3c space group). [28] We also verified that the formation process of Cs_4PbI_6 is directly formed from the precursor solution, instead of the solid-phase reaction between $CsPbI_3$ and the excessive CsI (Fig. S11–S13). For clearer visualization, the 1D diffraction pattern derived from 2D GIWAXS patterns was integrated in Fig. 2e and Table S3. Apparently, by increasing CsI/PbI_2 ratio from 1 to 1.5, the intensity ratio of (110) plane of γ-$CsPbI_3$ was enhanced accordingly, reaching the maximum at 1.1 CsI/PbI_2 ratio and then declined due to too much generated Cs_4PbI_6 phase at 1.5 CsI/PbI_2, which were summarized in Table S4. Besides that, excessive CsI changed the preferred stacking

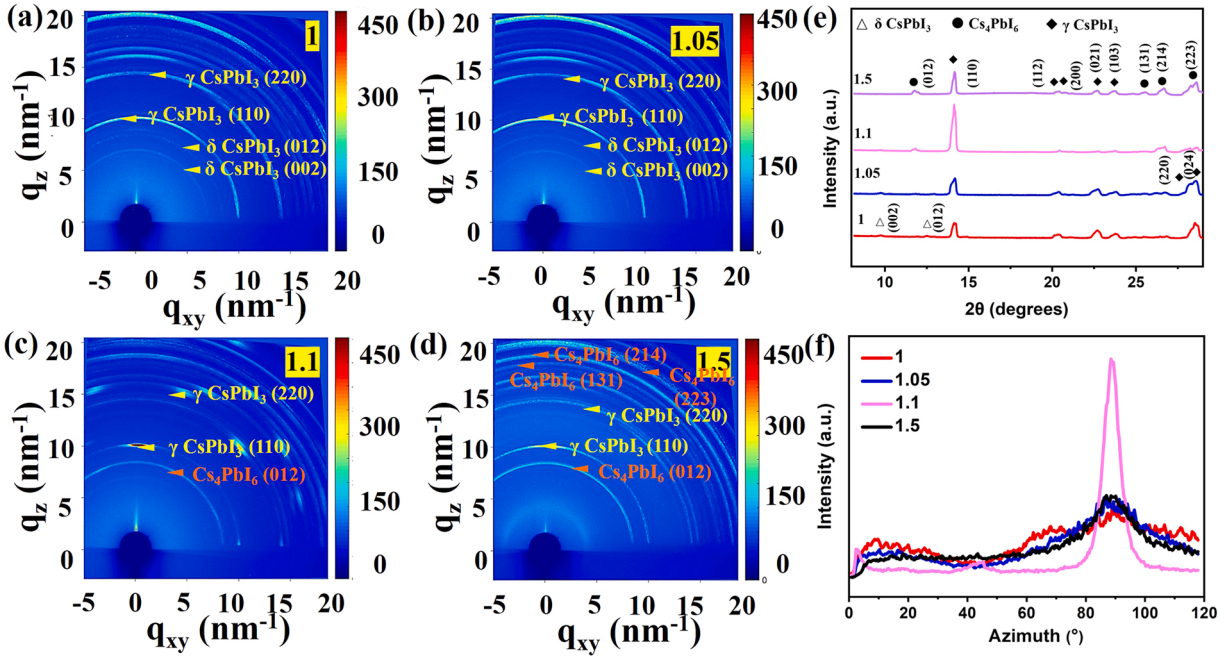

Fig. 2. (a–d) GIWAXS patterns for perovskite films with different CsI/PbI_2 ratio: a) 1, b) 1.05, c) 1.1, d) 1.5. e) 1D GIWAXS 2θ signals generated from 2D GIWAXS patterns (a–d). f) Integrated intensity plots generated from 2D GIWAXS patterns (a–e) along the ring at q = 10 nm^{-1}, assigned to the perovskite (110) plane.

orientation and promoted the growth of the γ-$CsPbI_3$ (110) plane along the out–of–plane direction, which was integrated in Fig. 3f. For the reference and 1.05, 1.5 CsI/PbI_2, the integrated curves exhibit almost a horizontal line with small protuberances at azimuth angles of 25°, 60° and 90°, revealing a relatively disordered crystal stacking within the perovskite thin films. For 1.1 CsI/PbI_2 ratio, the convex area at an azimuth angle of 90° presented, suggesting the increased probability for (110) plane stacking along the out-of-plane direction. [29] The 1.1 CsI/PbI_2 stoichiometry is beneficial for fabricating highly crystalline perovskite thin films with long-range order, instead of a relatively

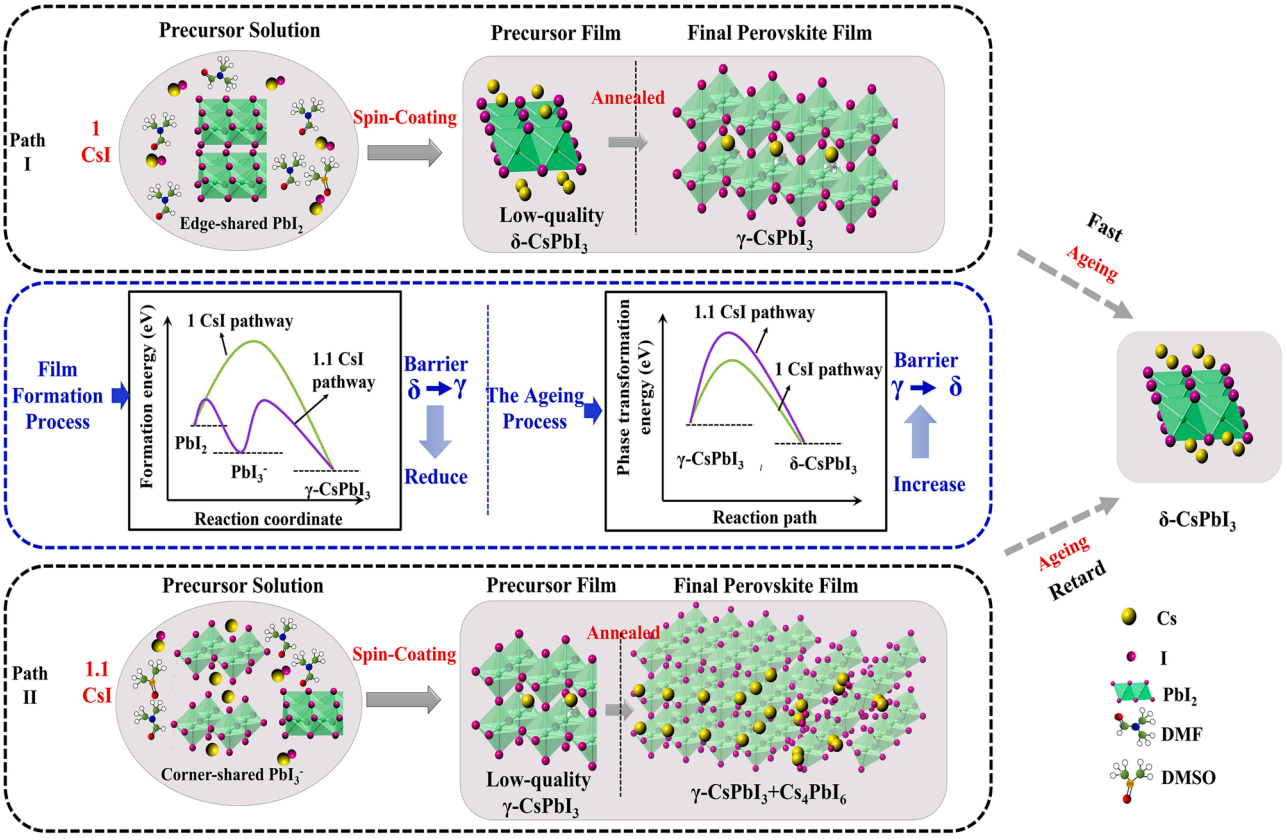

Fig. 3. Proposed mechanism diagram of $CsPbI_3$ crystal formation from precursor solution with the excessive CsI over a stoichiometric ratio of 1.

disordered crystal structure for the reference or 1.05, 1.5 CsI/PbI_2. As the microstructure arrangement was closely related to the optoelectronic properties of perovskite based thin films or devices, [30] we expect that the different preferred crystal orientations could in part account for the varied performance of solar cells with excessive CsI. The state of the final films after the annealing process was also investigated by UV−vis measurement (Fig. S14). Except for the reference with merely black phase $CsPbI_3$, all other samples have two peaks at 380 nm (Cs_4PbI_6) and 710 nm (black phase $CsPbI_3$). [31] Furthermore, the stoichiometric ratios of CsI/PbI_2 in the final films basically match with that in the precursors, which were verified by the X − ray photoelectron spectroscopy (XPS) analyses (Fig. S15 and Table S5).

A conceivable mechanism that CsI induced the phase transformation kinetics is proposed based on the above experimental facts and theoretical calculations [Fig. S3–S5]. It is known that when PbI_2 dissolved in the solution with DMF as major solvent, it stacks together via van der Waals interactions due to its inherent 2D nature. [28] With the subsequent incorporation of the same proportion CsI (1 CsI/PbI_2), most of the Cs^+ couldn't intercalated into the PbI_2 −DMF framework. In this case, the δ-phase is preferably formed in the precursor film. As the amount of CsI increasing, in other words, for 1.1 CsI/PbI_2, it will drive more Cs^+ intercalated into the PbI_2 framework, thereby promoting the formation of more PbI_3^- complex. Formation of more PbI_3^- could also enable stronger interaction between Cs^+ and the inorganic frameworks. This will allow a considerable quantity of perovskite structure pre-formed in the solution state, which substantially facilitate the phase transition from δ to γ, affording the favorable formation of γ phase. The morphology/composition evolution of the $CsPbI_3$ film with different excessive CsI was further investigated (Fig. S16–S18). For 1 CsI/PbI_2, the film is very rough with visible unevenness on millimeter scale. Conversely, with the increase of excessive CsI, a uniform and shiny perovskite film can be obtained. Moreover, newly formed species appeared in adjacent grains in the perovskite film (Fig. S16–S17). Through the Energy-dispersive X-ray spectroscopy (Fig. S18 and Table S6), the I/Pb ratio of the newly formed species (part B) was about ~6.23, much higher than that in other parts (part A). These species are speculated to be Cs_4PbI_6, as indicated in the GIWAXS, UV−vis measurement above. Subsequently, we have done stability test under high humidity (40%RH) to verify whether the Cs_4PbI_6 phase at the grain boundary helps stabilize the γ phase $CsPbI_3$. As shown in Fig. S19, the 1.1 CsI/PbI_2 and 1.5 CsI/PbI_2 film can partially retain black γ phase after storing in an air glovebox with a relative humidity of 40% at room temperature for half an hour, while other films, especially the pure $CsPbI_3$ film, turn into complete yellow δ phase. It indicates that the excessive CsI in the precursor solution would eventually form Cs_4PbI_6 structure, which could serve as a wrapping layer on the formed γ-$CsPbI_3$ phase, inhibiting the phase transition from γ to δ phase during the film ageing process. Therefore, by fine tuning the precursor stoichiometry, we are able to modulate phase transformation kinetics during film formation and ageing process.

Fig. 4a−b show the schematic diagram of the $CsPbI_3/Cs_4PbI_6$ structure, in which yellow color represents the wide bandgap (3.4 eV) Cs_4PbI_6 at grain boundaries (GBs), while green color represents the narrow bandgap (1.7 eV) $CsPbI_3$ grains (GIs). Scanning kelvin probe microscopy (SKPM) was further employed to examine the potentials difference between the $CsPbI_3$ grain and GBs (Fig. 4c−d and Fig. S20). For 1 CsI/PbI_2 and 1.1 CsI/PbI_2, we draw straight lines across grain/grain boundary at three different regions, defined as 1, 2, and 3 in the AFM and SKPM images, respectively. The pure $CsPbI_3$ film exhibits a higher surface potential at the GBs than that at the GIs for around 15 mV, hindering the extraction of holes, which is consistent with the previous observation in the hybrid perovskite solar cells. [30] In contrast, for the 1.1 CsI/PbI_2, the surface potential values at the GBs are

Table 1
The contact potential difference (CPD) and work function of 1.1 CsI/PbI_2 perovskite film.

Sample	CPD/mV (average)	Work Function /eV (average)
Part 1:GB	455	4.596
Part 1: GI	477	4.573
Part 2: GB	454	4.597
Part 2: GI	468	4.583
Part 3: GB	452	4.599
Part 3: GI	473	4.578

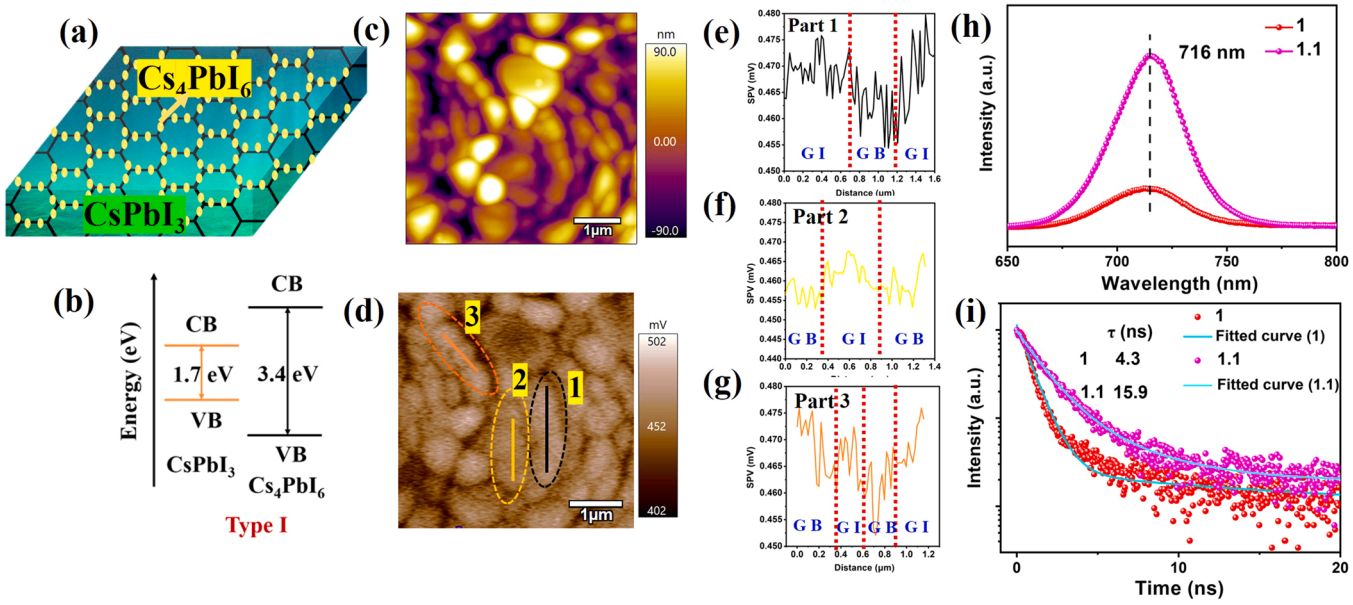

Fig. 4. (a) The schematic diagram of in-situ Cs_4PbI_6 passivated $CsPbI_3$ film, yellow color represents the wide bandgap Cs_4PbI_6 at GBs, green color represents the narrow bandgap $CsPbI_3$ grain. b) The coexistence of Cs_4PbI_6 and perovskite in the film shows a type I alignment of the band edge, with the band gap of 3.4 and 1.7 eV, respectively. c) AFM image. d) Two−dimensional surface potential spatial maps of 1.1 CsI/PbI_2 perovskite film, scale bars is 1 μm. e−g) 1D line profiles of the corresponding $CsPbI_3$ film. h) the steady photoluminescence spectra (PL). i) Time-resolved photoluminescence (TRPL) spectra of the perovskite films with different CsI/PbI ratios (1 and 1.1).

of a distinct 20 mV lower than that of the GIs on average (Fig. 4e–g and Table 1), leading to upward bending and facilitated hole extraction, which is possibly resulted from newly formed Cs_4PbI_6. To further study the recombination behavior of the photogenerated charge carriers in the reference and 1.1 CsI/PbI_2 films, we conducted steady–state and time–resolved photoluminescence (PL, TRPL) spectroscopy measurements. As shown in Fig. 4 h–i, only one PL peak located at 716 nm associated with γ-$CsPbI_3$ was observed, wherein no Cs_4PbI_6 signal was detected. While, the enhanced PL intensity and longer lifetime were observed in the 1.1 CsI/PbI_2 film that were believed to relate with the reduced carrier recombination. Also, space–charge limited current (SCLC) measurements were utilized to estimate the charge trap densities (Fig. S21 and Table S7). The measured V_{TFL} for the reference $CsPbI_3$ device was ~0.37 V, whereas the value decreased to 0.22 V for 1.1 CsI/PbI_2 device. Accordingly, a decrease of n_{trap} of ~1.46×10^{15} cm^{-3} for the 1.1 CsI/PbI_2 device was observed, compared with the control $CsPbI_3$ device (~2.46×10^{15} cm^{-3}), indicating the suppression of non-radiative recombination in the 1.1 CsI/PbI_2 device. [30] Therefore, the reduced carrier recombination could be attributed to the following two reasons: 1) the introduction of excessive CsI modulated the crystallization kinetics, resulting in improvement of optoelectronic properties, such as reduction of defect density; 2) the self-induced conversion of Cs_4PbI_6 effectively passivates the grain locally by forming type I alignment with $CsPbI_3/Cs_4PbI_6$, preventing carrier recombination from the surface defects and traps states.

We adopted these high-quality 1.1 CsI/PbI_2 perovskite films as absorber layers to fabricate solar cells by employing a typical planar configuration of ITO/SnO_2/perovskite/Spiro–MeOTAD/Au. From the SEM image (Fig. S22), the thicknesses of perovskite layer can be estimated to be about 400 nm. Fig. 5a and Fig. S23 showed the statistical distribution of PCE, J_{SC}, V_{OC}, and FF for these devices. The average PCE increased from ~12.8% to ~14.7% in the $CsPbI_3$ perovskite upon the introduction of excessive CsI. The champion 1.1 CsI/PbI_2 based PSC exhibits 15.13% efficiency over the 13.84% of 1 CsI/PbI_2 based PSC device (Fig. 5b and Table 2) , which can be mainly attributed to the enhancement of the FF from 70.9% to 75.09%, arising from the lower

Table 2
Photovoltaic parameters of the champion solar cells using 1 CsI/PbI_2, 1.1 CsI/PbI_2 perovskite film and CsI post–treatment 1.1 CsI/PbI_2 perovskite film as the absorber layers.

Device (X)	V_{OC} (V)	J_{SC} (mA/cm^2)	PCE (%)	FF (%)
1	1.063	18.36	13.84	70.9
1.1	1.074	18.77	15.13	75.09
CsI post–treatment	1.133	18.85	16.68	78.15

trap densities and longer carrier lifetime mentioned above. Furthermore, in order to further verify that the introduction of excessive CsI will improve the photoelectric performance, different processing steps were adopted to prepare perovskite absorber layers and the the corresponding solar cell were constructed, as shown in Fig. S24 and Table S8. To further strengthen the passivation effect, we coated an additional 2 mg/ml CsI/methonal (MeOH) solution onto the 1.1 CsI/PbI_2 film which was further annealed at 100 ℃ for 5 min. As shown in Fig. S25, no new phase such as Cs_4PbI_6 was formed, indicating that the post–treatment results in an excess amount of CsI onto the surface of perovskite layer. The neat methanol post–treated devices were fabricated, which show negligible difference in photovoltaic parameters compared with the untreated ones. as shown in Fig. S26 and Table S10. In contrast, a CsI/methanol solution could dramatically improve the photovoltaic parameters, particularly for FF and V_{OC}. This suggests the improvement of efficiency after CsI/methanol post-treatment is mainly due to the role of CsI instead of methanol. The champion device of 1.1 CsI/PbI_2 with CsI post treatment displayed an efficiency of 16.68% with a J_{SC} of 18.85 $mA{\cdot}cm^{-2}$, V_{OC} of 1.133 V, and FF of 78.15% under reverse scan (Fig. 5) and exhibited an efficiency of 16.31% with a J_{SC} of 19.34 mA cm^{-2}, V_{OC} of 1.11 V, FF of 75.85% under forward scan. Compared to the reference, the 1.1 CsI/PbI_2 device with the CsI post treatment also showed negligible *J–V* hysteresis (Fig. 5c and Table S9), resulting in a stable PCE output of 15.7% (Fig. 5d). Hysteresis index "H–index" was calculated and summarized in Table S9, and the H–index reduced significantly with CsI post treatment. Furthermore,

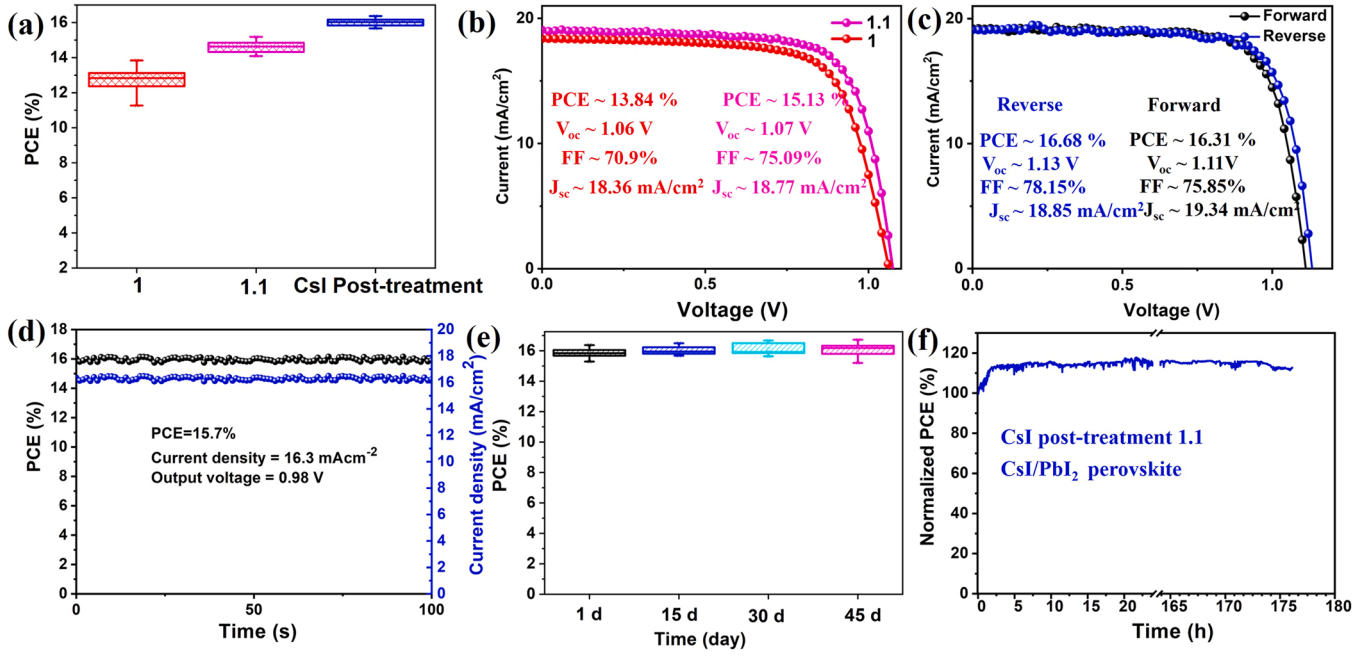

Fig. 5. Performance of inorganic perovskite solar cells. a) Statistics of PCE for devices using 1 CsI/PbI_2, 1.1 CsI/PbI_2 and CsI post–treatment 1.1 CsI/PbI_2 perovskite film as the absorber layers. b) *J–V* curves of the devices using 1 CsI/PbI_2, 1.1 CsI/PbI_2 perovskite film as the absorber layers. c) *J–V* curves of the device using CsI post–treatment 1.1 CsI/PbI_2 perovskite film as the absorber layers. d) The steady state output efficiency for the champion 1.1 CsI/PbI_2 perovskite film based PSC. e) Stability of CsI post–treatment 1.1 CsI/PbI_2 perovskite film based PSCs stored in the N_2 filled glovebox for 45 days. f) The MPP tracking of non–encapsulated CsI post–treatment 1.1 CsI/PbI_2 perovskite film based PSC measured under continuous white light LED illumination (100 $mW{\cdot}cm^{-2}$) in a N_2 glovebox.

the corresponding PSCs also exhibit higher reproducibility with a narrow PCE distribution (Fig. 5a) compared to the reference one. We speculate that the CsI passivation promotes the device performance by reducing carrier recombination at the interface of the absorber and transport layers. As shown in Fig. S27, this type I band alignment between CsI and $CsPbI_3$ forms energy barriers to prevent excitons from reaching the grain boundary trap states and defects, thus blocking the nonradiative channels [31,32]. Finally, the photovoltaic performance of ten of our best cells after 45 days storage in a glovebox were presented in Fig. 5e, demonstrating a commendable long durability. The slightly improved efficiency, rather than a dramatic drop, pointed out to a possible improved contact between hole transport layer and $CsPbI_3$ during storage, which assisted fast extraction of free carriers and thus enhanced performance of the PSCs. [33–35] Moreover, the 1.1 CsI/PbI_2 device with CsI post−treatment exhibited much improved stability with no performance loss for ~175 h MPP tracking under continuous illumination (white light LED source with a illumination spectrum within 400–700 nm, 100 $mW{\cdot}cm^{-2}$, Fig. S28) in a N_2 glovebox at 25 ℃. In contrast, the reference (Fig. S29) retained 80% of the initial PCE after 70 h. Therefore, excessive CsI precursor stoichiometry modulator can lead to a better control of the crystallization kinetics, accompanying with improved optoelectronic properties such as the suppression defect density of perovskite films.

3. Conclusion

In summary, we provide a full picture on how the stoichiometric ratio of CsI/PbI_2 impact the polyiodide complexes in the precursor solution, and phases evolution of $CsPbI_3$ during film formation and ageing, which is particularly aided by in-situ GIWAXS measurement. Different from intruding any foreign dopants, the excessive CsI itself could promote the favorable formation of black γ phase in the precursor film that aided by polyiodide complexes transferring from PbI_2 to PbI_3^- with Pb−I octahedral changed from edge sharing to corner sharing, in contrast to the overwhelming yellow δ-phase for 1 CsI/PbI_2. Moreover, the excessive CsI in precursor solution leads to Cs_4PbI_6 in the final film, which not only effectively passivates the grains to modify its photoelectric performance, but also retards the phase transformation from black γ to yellow δ phase. As a result, the optimized PSCs delivers both improved efficiency and stability, reaching 16.68% PCE without performance drop for ~175 h under continuous illumination. This work provides an effective means to tune the phase transformation barrier of $CsPbI_3$ films and highlights the importance of precursors chemistry on the fabrication of high-quality perovskite semiconductor.

4. Experimental section

4.1. Chemicals

The commercial chemical materials used were listed as follows: acetone (AR Beijing Chemical Works), ethanol (AR Beijing Chemical Works), isopropanol (99.99%, Sigma−Aldrich), CsI (99.99%, Sigma−Aldrich), PbI_2 (99.999%, Xi'an Polymer Light Technology Corp.), N, N − dimethylformamide (DMF; 99.99%, Sigma−Aldrich), Dimethyl sulfoxide (DMSO, 99.99%, Sigma−Aldrich), SnO_2 colloid precursor (Alfa Aesar, 15% in H_2O colloidal dispersion), chlorobenzene (99.9%, Sigma−Aldrich), Spiro−OMeTAD (99.9%, Xi'an Polymer Light Technology Corp.) and PCBM (99%, Xi'an Polymer Light Technology Corp.) were used directly without any purification.

4.2. Device fabrication

ITO−coated glass substrates were ultrasonically cleaned by detergent solution, deionized water, acetone, and ethanol for 15 mins each, and then dried with nitrogen blowing. A compact ~30 nm SnO_2 film was coated on UV−O_3 pre−treated ITO substrate. $CsPbI_3$ precursor solution (0.65 M) was prepared by dissolving CsI and PbI_2 in DMF and DMSO (DMF:DMSO=30:1) with different molar ratios of 1:1, 1.05:1, 1.1:1, 1.5:1, perovskite precursors were spin−coated in a two−step process at speed of 1000 and 2000 rpm for 3 s and 25 s, respectively. The obtained perovskite films were annealed at 320 ℃ for 3 mins. After cooling down to room temperature, a hole transport layer (HTL) was formed onto a top $CsPbI_3$ films by spin−coating a HTL solution at 3000 rpm for 30 s. The HTL solution was prepared by dissolving 72.3 mg Spiro–OMeTAD in 1 ml chlorobezene with additives of 30 μL tert–butylpyridine (TBP) and 35 μL Libis (trifluoromethanesulfonyl) imide (Li–TFSI). Finally, a 100 nm thick gold electrode was deposited by thermal evaporation through a shadow mask. The optical active layer of the solar cells is 0.08313 cm^2. All the fabrication steps were conducted in a nitrogen-filled glovebox except for the fabrication process of SnO_2 layer.

4.3. Characterization

The SEM images were acquired by using a field–emission scanning electron microscopy (SEM, Hitachi S–4800), using an electron beam accelerated at 500 V to 30 kV, enabling operation at a variety of currents. One dimensional X–ray diffraction (XRD) spectra was obtained by using Rigaku D/MAX 2400 diffractometer using Cu Kα radiation (λ = 1.5405 Å) as the X–ray source. The UV–vis absorption spectra of the samples was obtained by an UV–visible diffuse reflectance spectrophotometer (UV–vis DRS, Japan Hitachi UH4150). Two−dimensional synchrotron radiation grazing incidence wide-angle X–ray scattering (GIWAXS) were performed at BL14B beamline, Shanghai synchrotron Radiation Facility with a wavelength of 0.6887 Å to analyze the crystallinity and orientation within the perovskite films. 2D GIWAXS data were acquired by using a MarCCD with a distance c.a. 450 mm from the samples. Atomic force microscopy (AFM) measurements (Bruker Dimension Icon) were conducted to investigate roughness of $CsPbI_3$ films. PL testing was based on the FLS980 (Edinburgh Instruments Ltd) with an excitation at 470 nm. The UV–vis absorption spectra of the samples were obtained by an UV–visible diffuse reflectance spectrophotometer (UV–vis DRS, Japan Hitachi UH4150). *J–V* characteristics of photovoltaic devices were obtained by using a Keithley 2400 source meter under simulated one–sun AM 1.5 G illumination (100 mW cm^{-2}) from an Oriel 300 solar simulator. The J–V measurements were carried out in a N_2 glovebox. For UV–vis absorption measurement: To be noted, the above precursor solutions is diluted (10 μL in 5 ml DMF) to clearly reveal the presence of PbI_2, PbI_3^-, PbI_4^{2-} by avoiding the strong absorption of PbI_2. For GIWAXS measurements: In order to shorten the detection time, the CsI/PbI_2 precursor film was spin-coated in advance, and placed in a glove box for 45 min, and then experienced dynamic observation for 240 s using GIWAXS technique.

CRediT authorship contribution statement

Zhiwen Qiu: Conceptualization, Methodology, Funding acquisition, Writing – review & editing, **Feng Wang:** Writing – review & editing, Data curation, **Chenyue Wang:** Data curation, **Cheng Zhu:** Data curation, **Hao Wang:** Software, **Qi Chen:** Formal analysis, **Yihua Chen:** Investigation, Validation, **Yu Zhang:** Investigation, Validation, **Zhenyu Guo:** Writing – review & editing, **Nengxu Li:** Investigation, Validation, **Huachao Zai:** Investigation, Validation, **José Manuel Vicent-Luna:** Resources, Software, **Shuxia Tao:** Resources, Software, **Huanping Zhou:** Supervision, Project administration, Funding acquisition, Writing – review & editing.

Declaration of Competing Interest

The authors declare that they have no known competing financial interests or personal relationships that could have appeared to influence the work reported in this paper.

Acknowledgements

This work was supported by the National Key Research and Development Program of China (Grant No. 2020YFB1506400, 2017YFA0206701), the National Natural Science Foundation of China (Grant No. 51972004), and the Tencent Foundation through the XPLORER PRIZE, the Postdoctoral Science Foundation of China (Grant No. 2019M650334, 2020M670040) and Postdoctoral Science Special Foundation of China (Grant No.2020T130003).

Appendix A. Supporting information

Supplementary data associated with this article can be found in the online version at doi:10.1016/j.nanoen.2022.107388.

References

[1] D. Bi, C. Yi, J. Luo, J.-D. Décoppet, F. Zhang, S.M. Zakeeruddin, X. Li, A. Hagfeldt, M. Grätzel, Polymer-templated nucleation and crystal growth of perovskite films for solar cells with efficiency greater than 21%, Nature Energy 1 (2016) 16142.
[2] N. Pellet, P. Gao, G. Gregori, T.Y. Yang, M.K. Nazeeruddin, J. Maier, M. Grätzel, Mixed-organic-cation Perovskite photovoltaics for enhanced solar-light harvesting, Angew. Chem. Int. Ed. 126 (2014) 3215–3221.
[3] Q. Ye, Y. Zhao, S. Mu, P. Gao, X. Zhang, J. You, Stabilizing the black phase of cesium lead halide inorganic perovskite for efficient solar cells, Science China, Chemistry 62 (2019) 810–821.
[4] J.K. Nam, S.U. Chai, W. Cha, Y.J. Choi, W. Kim, M.S. Jung, J. Kwon, D. Kim, J. H. Park, Potassium incorporation for enhanced performance and stability of fully inorganic cesium lead halide perovskite solar cells, Nano Lett. 17 (2017) 2028–2033.
[5] G.E. Eperon, G.M. Paterno, R.J. Sutton, A. Zampetti, A.A. Haghighirad, F. Cacialli, H.J. Snaith, Inorganic cesium lead iodide perovskite solar cells, J. Mater. Chem. A 3 (2015) 19688–19695.
[6] C.C. Stoumpos, C.D. Malliakas, M.G. Kanatzidis, Semiconducting tin and lead iodide perovskites with organic cations: phase transitions, high mobilities, and near-infrared photoluminescent properties, Inorg. Chem. 52 (2013) 9019–9038.
[7] P. Wang, X. Zhang, Y. Zhou, Q. Jiang, Q. Ye, Z. Chu, X. Li, X. Yang, Z. Yin, J. You, Solvent-controlled growth of inorganic perovskite films in dry environment for efficient and stable solar cells, Nature, Communications 9 (2018) 2225–2231.
[8] Y. Zhao, Y. Wang, X. Liu, T. Zhang, X. Wang, M. Kan, J. Shi, The role of dimethylammonium iodide in $CsPbI_3$ perovskite fabrication: additive or dopant? Angew. Chem. Int. Ed. 58 (2019) 16691–16696.
[9] G.E. Eperon, G.M. Paterno, R.J. Sutton, A. Zampetti, A.A. Haghighirad, F. Cacialli, H.J. Snaith, Inorganic cesium lead iodide perovskite solar cells, J. Mater. Chem. A 3 (2015) 19688–19695.
[10] W. Ke, I. Spanopoulos, C.C. Stoumpos, M.G. Kanatzidis, Myths and reality of HPbI 3 in halide perovskite solar cells, Nature, Communications 9 (2018) 4785–4793.
[11] R.E. Beal, D.J. Slotcavage, T. Leijtens, A.R. Bowring, R.A. Belisle, W.H. Nguyen, G. F. Burkhard, E.T. Hoke, M.D. McGehee, Cesium lead halide perovskites with improved stability for tandem solar cells, J. Phys. Chem. Lett. 7 (2016) 746–751.
[12] C. Liu, W. Li, C. Zhang, Y. Ma, J. Fan, Y. Mai, All-inorganic $CsPbI_2Br$ perovskite solar cells with high efficiency exceeding 13%, J. Am. Chem. Soc. 140 (2018) 3825–3828.
[13] C. Liu, W. Li, J. Chen, J. Fan, Y. Mai, R.E. Schropp, Ultra-thin MoO_x as cathode buffer layer for the improvement of all-inorganic $CsPbIBr_2$ perovskite solar cells, Nano Energy 41 (2017) 75–83.
[14] G. Yin, H. Zhao, H. Jiang, S. Yuan, T. Niu, K. Zhao, Z. Liu, S. Liu, Precursor engineering for all-inorganic $CsPbI_2Br$ perovskite solar cells with 14.78% efficiency, Adv. Funct. Mater. 28 (2018) 1803269.
[15] W. Chen, H. Chen, G. Xu, R. Xue, S. Wang, Y. Li, Y. Li, Precise control of crystal growth for highly efficient $CsPbI_2Br$ perovskite solar cells, Joule 3 (2019) 191–204.
[16] C.Y. Chen, H.Y. Lin, K.M. Chiang, W.L. Tsai, Y.C. Huang, C.S. Tsao, H.W. Lin, All-vacuum-deposited stoichiometrically balanced inorganic cesium lead halide perovskite solar cells with stabilized efficiency exceeding 11%, Adv. Mater. 29 (2017) 1605290.
[17] C.F.J. Lau, M. Zhang, X. Deng, J. Zheng, J. Bing, Q. Ma, J. Kim, L. Hu, M.A. Green, S. Huang, A. Ho-Baillie, Strontium-doped low-temperature-processed $CsPbI_2Br$ perovskite solar cells, ACS Energy Lett. 2 (2017) 2319–2325.
[18] Y. Hu, F. Bai, X. Liu, Q. Ji, X. Miao, T. Qiu, S. Zhang, Bismuth incorporation stabilized α-$CsPbI_3$ for fully inorganic perovskite solar cells, ACS Energy Lett. 2 (2017) 2219–2227.
[19] Q. Wang, X. Zheng, Y. Deng, J. Zhao, Z. Chen, J. Huang, Bismuth incorporation stabilized α-$CsPbI_3$ for fully inorganic perovskite solar cells, Joule 2 (2017) 2219–2227.
[20] Y. Wang, T. Zhang, M. Kan, Y. Li, T. Wang, Y. Zhao, Efficient α-$CsPbI_3$ photovoltaics with surface terminated organic cations, Joule 2 (2018) 2065–2075.
[21] P. Becker, J.A. Márquez, J. Just, A. Al-Ashouri, C. Hages, H. Hempel, M. Jošt, S. Albrecht, R. Frahm, T. Unold, Low temperature synthesis of stable γ-$CsPbI_3$ perovskite layers for solar cells obtained by high throughput experimentation, Advanced Energy, Materials 9 (2019) 1900555.
[22] Y. Wang, T. Zhang, M. Kan, Y. Li, T. Wang, Y. Zhao, Efficient α-$CsPbI_3$ photovoltaics with surface terminated organic cations, Joule 2 (2018) 2065–2075.
[23] F. Bai, J. Zhang, Y. Yuan, H. Liu, X. Li, C.C. Chueh, H. Yan, Z. Zhu, A.K.Y. Jen, A 0D/3D heterostructured all-inorganic halide perovskite solar cell with high performance and enhanced phase stability, Adv. Mater. 31 (2019) 1904735.
[24] Z. Shao, H. Meng, X. Du, X. Sun, P. Lv, C. Gao, Y. Rao, C. Chen, Z. Li, X. Wang, Cs_4PbI_6-Mediated Synthesis of Thermodynamically Stable $FA_{0.15}Cs_{0.85}PbI_3$ Perovskite Solar Cells, Adv. Mater. 32 (2020) 2001054.
[25] J.M. Vicent-Luna, S. Apergi, S. Tao, Efficient computation of structural and electronic properties of halide perovskites using density functional tight binding: GFN1-xTB method, J. Chem. Inf. Model. 61 (2021) 4415.
[26] K. Yan, M. Long, T. Zhang, Z. Wei, H. Chen, S. Yang, J. Xu, Hybrid halide perovskite solar cell precursors: colloidal chemistry and coordination engineering behind device processing for high efficiency, J. Am. Chem. Soc. 137 (2015) 4460–4468.
[27] M. Jung, S.-G. Ji, G. Kim, S.I. Seok, Perovskite precursor solution chemistry: from fundamentals to photovoltaic applications, Chem. Soc. Rev. 48 (2019) 2011–2038.
[28] J.A. Steele, H. Jin, I. Dovgaliuk, R.F. Berger, T. Braeckevelt, H. Yuan, C. Martin, E. Solano, K. Lejaeghere, S.M. Rogge, Thermal unequilibrium of strained black CsPbI3 thin films[J], Science 365 (2019) 679–684.
[29] Y. Wang, M.I. Dar, L.K. Ono, T. Zhang, M. Kan, Y. Li, L. Zhang, X. Wang, Y. Yang, X. Gao, Thermodynamically stabilized β-$CsPbI_3$–based perovskite solar cells with efficiencies> 18%, Science 365 (2019) 591–595.
[30] G. Zheng, C. Zhu, Y. Chen, J. Zhang, Q. Chen, X. Gao, H. Zhou, Microstructure variations induced by excess PbX_2 or AX within perovskite thin films, Chem. Commun. 53 (2017) 12966–12969.
[31] Y. Zhang, C. Wu, D. Wang, Z. Zhang, X. Qi, N. Zhu, G. Liu, X. Li, H. Hu, Z. Chen, L. Xiao, B. Qu, High Efficiency (16.37%) of Cesium Bromide-Passivated All-Inorganic $CsPbI_2Br$ Perovskite Solar Cells, Sol. RRL 3 (2019) 1900254.
[32] S. Yang, W. Liu, Y. Han, Z. Liu, W. Zhao, C. Duan, Y. Che, H. Gu, Y. Li, S. Liu, 2D $Cs_2PbI_2Cl_2$ Nanosheets for Holistic Passivation of Inorganic $CsPbI_2Br$ Perovskite Solar Cells for Improved Efficiency and Stability, Adv. Energy Mater. 10 (2020) 2002882.
[33] Z. Xu, Z. Liu, N. Li, G. Tang, G. Zheng, C. Zhu, Y. Chen, L. Wang, Y. Huang, L. Li, A thermodynamically favored crystal orientation in mixed formamidinium/methylammonium perovskite for efficient solar cells, Adv. Mater. 31 (2019) 1900390.
[34] F. Hao, C.C. Stoumpos, Z. Liu, R.P. Chang, M.G. Kanatzidis, Controllable perovskite crystallization at a gas–solid interface for hole conductor-free solar cells with steady power conversion efficiency over 10%, J. Am. Chem. Soc. 136 (2014) 16411–16419.
[35] Q. Chen, H. Zhou, T.-B. Song, S. Luo, Z. Hong, H.-S. Duan, L. Dou, Y. Liu, Y. Yang, Controllable self-induced passivation of hybrid lead iodide perovskites toward high performance solar cells, Nano Lett. 14 (2014) 4158–4163.

Zhiwen Qiu received her Ph.D. degrees from the School of Material Science and Engineering under joint supervision of Prof. Bingqiang Cao from University of Jinan and Huanping Zhou from Peking University. She is currently a postdoctoral fellow in the College of Engineering, Peking University. Her current research interest is developing high-efficiency and stable inorganic perovskite solar cells.

Feng Wang received his Ph.D. from University of Electronic Science and Technology of China in 2019 working on crystallization behaviour of lead halide perovskites in ambient air. He is currently a postdoc at Peking University, focusing on inorganic perovskites and their optoelectronic applications.

Chenyue Wang received his B.S. degree from University of Science and Technology Beijing in 2018, and received his M.S. degree from Beijing Institute of Technology in 2021. Now he is Ph.D. candidate under the supervision of Prof. Xingyu Gao in Shanghai Synchrotron Radiation Facility (SSRF), Shanghai Advanced Research Institute, Chinese Academy of Sciences. His research focuses on the fabrication and characterization of perovskite solar cells.

Cheng Zhu received his Ph.D. degree in 2021 from School of Materials Science & Technology, Beijing Institute of Technology, majored in Materials Science and Engineering. His current research interest is exploring microstructure optimization (including orientation, strain, etc.) of perovskite materials to improve device efficiency and long-term stability.

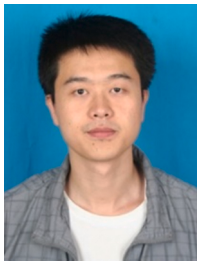

Hao Wang received his Ph.D. degree in Materials Science and Engineering from Beijing Institute of Technology in 2020. Now, he is working as a postdoctoral fellow with Prof. Qi Chen and Pengwan Chen in the School of Materials Science & Engineering, Beijing Institute of Technology. His research focuses on perovskite solar cells and nanomaterials.

Qi Chen holds both his B.S and M.S degrees in Tsinghua University, and received his Ph.D. degree at University of California, Los Angeles (UCLA). From 2013–2016, he worked as a postdoc fellow at California Nanosystem Institute (CNSI), UCLA, with Prof. Yang Yang's supervision. Now he is the professor in Beijing Inistitute of Technology. His research focuses on hybrids materials design, processing and applications in opto-electronics and for energy harvesting and storage.

Yihua Chen received his B.S degrees in School of materials science and engineering from Beijing Institute of Technology in 2016, majored in Materials Chemistry. He received his Ph.D. degree in 2021 from College of Engineering, Peking University. His current research interest is developing new materials and techniques for high efficiency silicon-perovskite and perovskite-perovskite tandem solar cells.

Yu Zhang received his B.S. degree in 2018 from College of Engineering, Peking University, majored in Materials science and engineering. And now he is Ph.D. candidate under the supervision of Prof. Huanping Zhou in School of Materials Science and Engineering, Peking University. His current research interest is developing high-efficiency and stable perovskite solar cells.

Zhenyu Guo received his B.S. degree in 2018 from School of Materials science and Engineering, Tianjin University. And now he is Ph.D. candidate under the supervision of Prof. Huanping Zhou in School of Materials Science and Engineering, Peking University. His current research interest is developing high-efficiency and stable perovskite light-emitting diodes.

Nengxu Li received his B.S. degree in 2017 from School of Materials Science & Technology, University of Science and Technology of China, majored in Materials Chemistry. And now he is Ph.D. candidate under the supervision of Prof. Huanping Zhou in College of Engineering, Peking University. His current research interest is developing high-efficiency and stable perovskite solar cells.

Shuxia Tao is working on Computational Materials Physics at the Center for Computational Energy Research, Applied Physics, Eindhoven University of Technology (TU/e), the Netherlands. With a Physical Chemistry background from Nankai University in China, Shuxia Tao started her PhD in 2007 at Department of Chemical Engineering and Chemistry, TU/e, the Netherlands. There she learnt Computational Materials Science and earned her PhD in 2011 with a thesis on hydrogen storage in metal hydrides for battery applications. After a short career break to care for her children, from 2013 to 2016, she worked as a post-doctoral researcher at NWO physics institute NIKHEF for computational materials design for photodetectors.

Huanping Zhou received Ph.D. in inorganic chemistry from Peking University, in 2010. After that, she joined University of California, Los Angeles, as a postdoctoral researcher from 2010 to 2015. From July 2015, she joined Peking University as a professor in Department/School of Materials Science and Engineering. She is a materials chemist with expertise in the fields of nanoscience, thin-film optoelectronic materials, and the development and fabrication of related devices, such as PV cells, LEDs, etc. Currently, her group focuses on thin-film optoelectronics, e.g., perovskite materials and solar cells.